Bifurcation-based shimmy analysis of landing gears using flexible multibody models

Beckers, C. J.J.; Öngüt, A. E.; Verbeek, G.; Fey, R. H.B.; Lemmens, Y.; van de Wouw, N.

DOI
10.1007/978-3-030-13317-7_7

Publication date
2019

Document Version
Final published version

Published in
Nonlinear Structural Dynamics and Damping

Citation (APA)
Beckers, C. J. J., Öngüt, A. E., Verbeek, G., Fey, R. H. B., Lemmens, Y., & van de Wouw, N. (2019). Bifurcation-based shimmy analysis of landing gears using flexible multibody models. In J. C. Jauregui (Ed.), *Nonlinear Structural Dynamics and Damping* (pp. 261-291). (Mechanisms and Machine Science; Vol. 69). Springer. https://doi.org/10.1007/978-3-030-13317-7_7

Chapter 7
Bifurcation-Based Shimmy Analysis of Landing Gears Using Flexible Multibody Models

C. J. J. Beckers, A. E. Öngüt, G. Verbeek, R. H. B. Fey, Y. Lemmens and N. van de Wouw

Abstract Shimmy oscillations are undesired vibrations in aircraft landing gears. In this chapter, the onset of shimmy vibrations, marked by Hopf bifurcations, is investigated in the parameter space of high-fidelity, flexible multibody landing gear models. Such a bifurcation analysis is performed by combining the Virtual.Lab Motion multibody solver with the numerical continuation software AUTO. The resulting quasi-2-parameter bifurcation diagrams, involving aircraft velocity and normal load, are verified using conventional time-simulation methods and are shown to be computationally more efficient. A sensitivity study reveals the influence of design parameters, such as the shimmy damping coefficient, mechanical trail, and steering actuator stiffness, on the occurrence of shimmy.

Keywords Bifurcation analysis · Flexible multibody dynamics · Shimmy · Landing gear dynamics

---

C. J. J. Beckers · R. H. B. Fey (✉) · N. van de Wouw
Dynamics and Control Group, Department of Mechanical Engineering, Eindhoven University of Technology, Eindhoven, The Netherlands
e-mail: R.H.B.Fey@tue.nl

N. van de Wouw
Department of Civil, Environmental and Geo-Engineering, University of Minnesota, Minneapolis, USA

N. van de Wouw
Delft Center for Systems and Control, Delft University of Technology, Delft, The Netherlands

A. E. Öngüt · Y. Lemmens
Siemens PLM Software, Leuven, Belgium

G. Verbeek
Fokker Landing Gear, Helmond, The Netherlands

J. C. Jauregui (ed.), *Nonlinear Structural Dynamics and Damping*,
Mechanisms and Machine Science 69,
https://doi.org/10.1007/978-3-030-13317-7_7

7.1 Introduction

Shimmy is a self-excited lateral-yaw oscillation of landing gear wheels that can occur during take-off, landing, or taxiing of an aircraft. In severe forms, it can cause discomfort for the pilot/passengers or even damage the safety-critical landing gear structure. Therefore, it is essential to assess the susceptibility of landing gears to shimmy early in the design process, preferably through model-based analysis.

Numerical continuation methods are often employed to analyse the Hopf bifurcations that mark the occurrence of shimmy in the parameter space of analytical models, such as in [7] and [13]. However, these models are often of limited complexity and represent significant simplifications of the complex landing gear structures. In contrast, the landing gear industry adopts time integration procedures for flexible multibody models, which can be highly complex and often include several types of nonlinearities and dynamic effects, such as mechanical free-play, flexible structures with large rotations/deformations, nonlinear dampers, contacts, and tires [9]. These multibody models form accurate representations of the actual landing gear dynamics, but the simulations are computationally expensive and only result in the stability properties of the landing gear at discrete points in the parameter space.

This study aims to bridge the gap between these analysis approaches and model types, by analyzing the shimmy stability properties of a complex, high-fidelity, flexible multibody landing gear model, as shown in Fig. 7.1, using numerical continuation software. The simulation framework developed in [11] is adapted to enable the analysis of larger, more complex models. With respect to this previous study, which analysed multibody models with up to 9 discrete degrees of freedom (DOFs), the

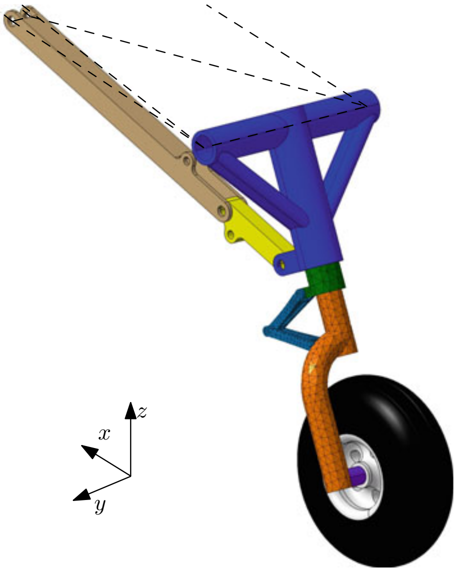

Fig. 7.1 Isometric view of the multibody landing gear model used in this study

model in Fig. 7.1 represents both the geometry and the dynamics of a real-world landing gear more accurately. The model is more complex, containing more bodies, some of which are considered flexible to account for the compliance of the landing gear structure. Modelling this compliance with flexible bodies, instead of using discrete rotational DOFs with a lumped stiffness, results in more realistic motions of the landing gear.

In this chapter, Sect. 7.2 summarizes the required preliminary theory for the description of the flexible multibody model, which also includes tire dynamics. In Sect. 7.3, the multibody landing gear model is explained, detailing the specific dynamics that are modeled, after which Sect. 7.4 provides an overview of the used simulation framework. The results of the analysis are discussed in Sect. 7.5 and the conclusions are summarized in Sect. 7.6. This work is an extended version of a conference paper [2], which focuses more on the applied simulation framework.

7.2 Preliminaries on Multibody Dynamics

The dynamics of a multibody system can be described by a system of differential-algebraic equations (DAE's) according to [6, p. 224]

$$\begin{cases} \begin{bmatrix} \underline{M}(\underline{q}) & \underline{\varPhi}^T_{,\underline{q}}(\underline{q},t) \\ \underline{\varPhi}_{,\underline{q}}(\underline{q},t) & 0 \end{bmatrix} \begin{bmatrix} \ddot{\underline{q}} \\ \underline{\lambda} \end{bmatrix} = \begin{bmatrix} \underline{Q}^A(\underline{q},\dot{\underline{q}}) + \underline{Q}^E(\dot{\underline{q}},\underline{q},t) \\ \underline{\gamma}(\dot{\underline{q}},\underline{q},t) \end{bmatrix}, \\ \underline{\varPhi}_{,\underline{q}}(\underline{q},t)\dot{\underline{q}} = -\frac{\partial\underline{\varPhi}(\underline{q},t)}{\partial t}, \\ \underline{\varPhi}(\underline{q},t) = \underline{0}, \end{cases} \tag{7.1}$$

where $\underline{M}$ is the mass matrix, which is a function of the column of generalized coordinates $\underline{q}$, $\underline{\varPhi}_{,\underline{q}}$ is the constraint Jacobian, where $_{,\underline{q}}$ denotes the partial derivative with respect to $\underline{q}$, and $\underline{\varPhi}$ reflects the holonomic constraints, $\underline{\lambda}$ is the associated column of Lagrange multipliers, and $\underline{Q}^A$ denotes the column of generalized applied forces. Additionally, in the Virtual.Lab Motion software [10], the column $\underline{Q}^E$ includes applied forces supplied by external sources, such as an external control system. The column $\underline{\gamma}$ defines the acceleration-level constraint equations, according to

$$\underline{\varPhi}_{,\underline{q}}(\underline{q},t)\ddot{\underline{q}} = -\left[\frac{\partial\left(\underline{\varPhi}_{,\underline{q}}(\underline{q},t)\dot{\underline{q}}\right)}{\partial\underline{q}} + 2\frac{\partial\underline{\varPhi}_{,\underline{q}}(\underline{q},t)}{\partial t}\right]\dot{\underline{q}} - \frac{\partial^2\underline{\varPhi}(\underline{q},t)}{\partial t^2} =: \underline{\gamma}(\dot{\underline{q}},\underline{q},t). \tag{7.2}$$

The second and third equalities in (7.1) represent the constraint equations on velocity and position level, respectively.

The generalized coordinates $\underline{q}$ consist of both dependent- and independent generalized coordinates, respectively $\underline{q}_D$ and $\underline{q}_I$, which are related through the constraint equations $\underline{\varPhi}(\underline{q},t) = \underline{0}$. The multibody solver of Virtual.Lab Motion, previously known as the DADS solver, and hereafter named the Motion solver, applies the so-called augmented formulation, i.e., rather than eliminating all redundant equations from the system before solving, the equations of motion are integrated in time with the redundant generalized coordinates and Lagrange multipliers included [8, p. 118]. Before integration, the second-order differential equations in (7.1) are transformed into a first-order form by introducing the state variable $\underline{x} = [\underline{x}_1^T \ \underline{x}_2^T]^T := [\underline{q}^T \ \underline{\dot{q}}^T]^T$. The dynamics in (7.1) can now be described in terms of the states $\underline{x}_1$, $\underline{x}_2$, $\underline{\lambda}$, and $\underline{\chi}$ as

$$\begin{bmatrix} \underline{I} & 0 & 0 & 0 \\ 0 & \underline{M}(\underline{x}_1) & \underline{\Phi}^T_{,\underline{x}_1}(\underline{x}_1, t) & 0 \\ 0 & \underline{\Phi}_{,\underline{x}_1}(\underline{x}_1, t) & 0 & 0 \\ 0 & 0 & 0 & \underline{I} \end{bmatrix} \begin{bmatrix} \underline{\dot{x}}_1 \\ \underline{\dot{x}}_2 \\ \underline{\lambda} \\ \underline{\dot{\chi}} \end{bmatrix} = \begin{bmatrix} \underline{x}_2 \\ \underline{Q}^A(\underline{x}_1, \underline{x}_2) + \underline{Q}^E(\underline{x}_1, \underline{x}_2, t) \\ \underline{\gamma}(\underline{x}_1, \underline{x}_2, t) \\ \underline{g}(\underline{x}_1, \underline{x}_2, \underline{\lambda}, \underline{\chi}) \end{bmatrix}, \quad (7.3)$$

which, in case of time-simulation, is integrated directly using one of the available numerical integration schemes [6, pp. 259–276]. The additional states $\underline{\chi}$ in (7.3) represent the dynamics of the system that are not directly a part of the multibody dynamics, e.g., the tire dynamics. The states in $\underline{x}$ corresponding to the positions and velocities of the independent generalized coordinates are indicated as $\underline{x}_I$.

7.2.1 Including Structural Compliance

The rigid multibody model can be extended by taking the structural flexibility of the bodies into account. A model derivation is provided below. A reference to [8, pp. 185–221], [14], and [15] is made for the full details.

7.2.1.1 Floating Frame of Reference Formulation

The floating frame of reference formulation is used. This implies that the displacements due to the elastic deformation of the flexible body are described with respect to a body-fixed reference frame, as shown in Fig. 7.2. Figure 7.2 shows an inertial reference frame $\{O^1, \underline{\vec{e}}^1\}$ and a flexible body B, which has a body-fixed reference frame $\{B, \underline{\vec{e}}^B\}$. The body reference frame position is defined by $\vec{r}_B$ and its orientation by a column of four Euler parameters $\underline{\theta}_B$, which defines the orientation of $\underline{\vec{e}}^B$ with respect to $\underline{\vec{e}}^1$.

The contribution of elastic deformation to the position of an arbitrary point i on the body, is given by

$$\vec{u}_i = \underline{u}_i^T \underline{\vec{e}}^B = \begin{bmatrix} u_1 \ u_2 \ u_3 \end{bmatrix}_i \begin{bmatrix} \vec{e}_1^B \\ \vec{e}_2^B \\ \vec{e}_3^B \end{bmatrix}, \quad (7.4)$$

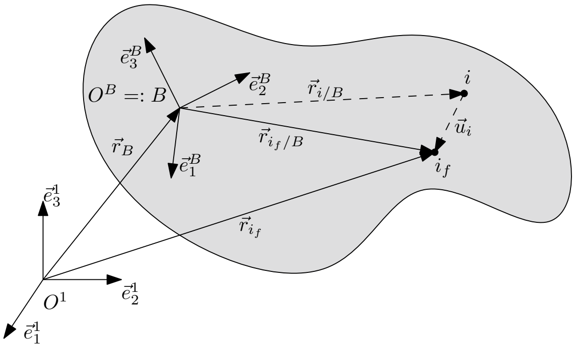

Fig. 7.2 Deformable body vector definitions

where $\underline{u}_i$ is the column with coordinates that defines $\vec{u}_i$ in the body reference frame. The position of point i in the deformed situation, point i_f, with respect to the origin of the body reference frame, is given by

$$\vec{r}_{i_f/B} = \vec{r}_{i/B} + \vec{u}_i \ , \tag{7.5}$$

where $\vec{r}_{i/B}$ is the position of point i with respect to B in the undeformed situation. The position of point i_f can also be expressed with respect to the inertial reference frame by

$$\begin{aligned} \vec{r}_{i_f} &= \vec{r}_B + \vec{r}_{i/B} + \vec{u}_i \\ &= \underline{\vec{e}}^{1^T} \underline{r}_B + \underline{\vec{e}}^{B^T} (\underline{r}_{i/B} + \underline{u}_i) \\ &= \underline{\vec{e}}^{1^T} \left(\underline{r}_B + \underline{A}^{1B}(\underline{r}_{i/B} + \underline{u}_i)\right) = \underline{\vec{e}}^{1^T} \underline{r}_{i_f} \ , \end{aligned} \tag{7.6}$$

where $\underline{A}^{1B}$ is the direction cosine matrix that defines the rotation from $\underline{\vec{e}}^B$ to $\underline{\vec{e}}^1$, according to

$$\underline{\vec{e}}^1 = \underline{A}^{1B} \underline{\vec{e}}^B \ . \tag{7.7}$$

This matrix is a function of the four Euler parameters: $A^{1B} = A^{1B}(\underline{\theta}_B)$.

The lumped mass formulation is used to describe the deformation of the flexible body. This implies that the body is approximated by a finite number of grid points. The mass of the body is lumped into the point masses of the grid points, or nodes. This approach enables us to express the deformation of one of the points, for instance point i, as function of a set of shape vectors $\underline{\psi}$ that describe the effect of the deformation on the position of the selected point. Therefore, the deformation coordinates in (7.4) can be described by

$$\underline{u}_i = \underline{\Psi}_i \underline{\eta}_B \ , \tag{7.8}$$

where $\underline{\Psi}_i$ is the $3 \times n_\eta$ matrix containing the modal displacements of point i, and $\underline{\eta}_B$ is the column containing the n_η modal coordinates used to describe the deformation of body B. Matrix $\underline{\Psi}_i$ is a row partition of the modal matrix $\underline{\Psi}$. This modal matrix describes the reduced elastic modes of all point on the body and is a result of modal reduction that will be described in Sect. 7.2.1.3.

By applying (7.8), the global coordinates of point i_f can be expressed as

$$\underline{r}_{i_f} = \underline{r}_B + \underline{A}^{1B}(\underline{\theta}_B)\left(\underline{r}_{i/B} + \underline{\Psi}_i \underline{\eta}_B\right) . \tag{7.9}$$

The global position of point i_f is now fully defined as function of the generalized coordinates of the body

$$\underline{q}_B = \begin{bmatrix} \underline{r}_B \\ \underline{\theta}_B \\ \underline{\eta}_B \end{bmatrix} , \tag{7.10}$$

which comprises the reference coordinates $\underline{r}_B$ and $\underline{\theta}_B$ and the modal coordinates $\underline{\eta}_B$. It is of importance that the modal coordinates $\underline{\eta}_B$ do not include the rigid body modes of the system, because these are already described by the reference coordinates.

The velocity of point i_f can be derived by differentiating (7.9) with respect to time and applying the chain rule

$$\dot{\underline{r}}_{i_f} = \dot{\underline{r}}_B + \dot{\underline{A}}^{1B}\left(\underline{r}_{i/B} + \underline{\Psi}_i \underline{\eta}_B\right) + \underline{A}^{1B}\underline{\Psi}_i \dot{\underline{\eta}}_B , \tag{7.11}$$

where the relation $\dot{\underline{r}}_{i/B} = 0$ has been used. In general, it is possible to rewrite the central term on the right hand side of (7.11) as

$$\dot{\underline{A}}^{1B}\left(\underline{r}_{i/B} + \underline{\Psi}_i \underline{\eta}_B\right) = \dot{\underline{A}}^{1B}\underline{r}_{i_f/B} = \underline{P}_i \dot{\underline{\theta}}_B , \tag{7.12}$$

where $\underline{P}_i = \underline{P}_i(\underline{\theta}_B, \underline{\eta}_B)$ is defined as

$$\underline{P}_i = \left[\frac{\partial}{\partial \theta_1}(\underline{A}^{1B}\underline{r}_{i_f/B}) \; \ldots \; \frac{\partial}{\partial \theta_4}(\underline{A}^{1B}\underline{r}_{i_f/B}) \right] , \tag{7.13}$$

which is a 3 × 4 matrix. Full details on how to assemble $\underline{P}_i$ in the particular situation that Euler parameters are used as rotational coordinates are stated in [14, p. 110]. Substituting (7.12) into (7.11) results in

$$\dot{\underline{r}}_{i_f} = \left[\underline{I} \;\; \underline{P}_i \;\; \underline{A}^{1B}\underline{\Psi}_i \right] \begin{bmatrix} \dot{\underline{r}}_B \\ \dot{\underline{\theta}}_B \\ \dot{\underline{\eta}}_B \end{bmatrix} . \tag{7.14}$$

7.2.1.2 Flexible Equations of Motion

Once the global position and velocity coordinates are known for all points in the body, the kinetic energy of the individual points can be summed to obtain the total kinetic energy of the body, according to

$$\begin{aligned} T_B &= \frac{1}{2}\sum_{i=1}^{n_n} m_i \begin{bmatrix} \dot{\underline{r}}_B \\ \dot{\underline{\theta}}_B \\ \dot{\underline{\eta}}_B \end{bmatrix}^T \begin{bmatrix} \underline{I} & \underline{P}_i & \underline{A}^{1B}\underline{\Psi}_i \\ & \underline{P}_i^T\underline{P}_i & \underline{P}_i^T\underline{A}^{1B}\underline{\Psi}_i \\ sym. & & \underline{\Psi}_i^T\underline{\Psi}_i \end{bmatrix} \begin{bmatrix} \dot{\underline{r}}_B \\ \dot{\underline{\theta}}_B \\ \dot{\underline{\eta}}_B \end{bmatrix} \\ &=: \frac{1}{2}\begin{bmatrix} \dot{\underline{r}}_B \\ \dot{\underline{\theta}}_B \\ \dot{\underline{\eta}}_B \end{bmatrix}^T \underline{M}_B(\underline{\theta}_B, \underline{\eta}_B) \begin{bmatrix} \dot{\underline{r}}_B \\ \dot{\underline{\theta}}_B \\ \dot{\underline{\eta}}_B \end{bmatrix} , \end{aligned} \tag{7.15}$$

where n_n is the total number of nodes of the body, m_i are the nodal masses, and $\underline{M}_B$ is the resulting mass matrix of the body. This mass matrix is a function of the rotational coordinates $\underline{\theta}_B$ and the modal coordinates $\underline{\eta}_B$.

The elastic strain energy of the body can be expressed as

$$U_B = \frac{1}{2}\begin{bmatrix} \underline{r}_B \\ \underline{\theta}_B \\ \underline{\eta}_B \end{bmatrix}^T \begin{bmatrix} 0 & 0 & 0 \\ 0 & 0 & 0 \\ 0 & 0 & \underline{K}^{red} \end{bmatrix} \begin{bmatrix} \underline{r}_B \\ \underline{\theta}_B \\ \underline{\eta}_B \end{bmatrix} , \tag{7.16}$$

where $\underline{K}^{red} = \underline{\Psi}^T\underline{K}\underline{\Psi}$ is the modal stiffness matrix and $\underline{K}$ is the structural stiffness matrix.

In case $\vec{F}_i = \underline{F}_i^T\underline{\vec{e}}^1$ is defined to be the net external force acting on node i of the body, the virtual work of all forces acting on the body can be written as

$$\delta W_B = \sum_{i=1}^{n_n} \underline{F}_i^T \delta\underline{r}_{i_f} . \tag{7.17}$$

Given the found relation for $\dot{\underline{r}}_{i_f}$ from (7.14), it can be concluded that

$$\delta\underline{r}_{i_f} = \begin{bmatrix} \underline{I} & \underline{P}_i & \underline{A}^{1B}\underline{\Psi}_i \end{bmatrix} \begin{bmatrix} \delta\underline{r}_B \\ \delta\underline{\theta}_B \\ \delta\underline{\eta}_B \end{bmatrix} . \tag{7.18}$$

Substituting (7.18) into (7.17) results the virtual work

$$\begin{aligned} \delta W &= \begin{bmatrix} \sum_{i=1}^{n_n} \underline{F}_i^T & \sum_{i=1}^{n_n} \underline{F}_i^T\underline{P}_i & \sum_{i=1}^{n_n} \underline{F}_i^T\underline{A}^{1B}\underline{\Psi}_i \end{bmatrix} \begin{bmatrix} \delta\underline{r}_B \\ \delta\underline{\theta}_B \\ \delta\underline{\eta}_B \end{bmatrix} \\ &=: \begin{bmatrix} (\underline{Q}_B^e)_r^T & (\underline{Q}_B^e)_\theta^T & (\underline{Q}_B^e)_\eta^T \end{bmatrix} \begin{bmatrix} \delta\underline{r}_B \\ \delta\underline{\theta}_B \\ \delta\underline{\eta}_B \end{bmatrix} =: (\underline{Q}_B^e)^T\delta\underline{q}_B , \end{aligned} \tag{7.19}$$

where $\underline{Q}_B^e$ is defined as the generalized forces acting on the body B for the three types of generalized coordinates. These typically include all forces due to spring, damper, and actuator elements.

Together with the obtained definitions for the kinetic energy T_B, the elastic strain energy U_B, and the generalized applied forces $\underline{Q}_B^e$, the use of Lagrange's equation results in the equations of motion of a single flexible body B, without constraint equations [14]:

$$\begin{bmatrix} \underline{m}_{rr} & \underline{m}_{r\theta} & \underline{m}_{r\eta} \\ & \underline{m}_{\theta\theta} & \underline{m}_{\theta\eta} \\ sym. & & \underline{m}_{\eta\eta} \end{bmatrix} \begin{bmatrix} \ddot{\underline{r}}_B \\ \ddot{\underline{\theta}}_B \\ \ddot{\underline{\eta}}_B \end{bmatrix} + \begin{bmatrix} 0 & 0 & 0 \\ 0 & 0 & 0 \\ 0 & 0 & \underline{K}^{red} \end{bmatrix} \begin{bmatrix} \underline{r}_B \\ \underline{\theta}_B \\ \underline{\eta}_B \end{bmatrix} = \begin{bmatrix} (\underline{Q}_B^e)_{r_B} \\ (\underline{Q}_B^e)_{\theta_B} \\ (\underline{Q}_B^e)_{\eta_B} \end{bmatrix} + \begin{bmatrix} (\underline{Q}_B^v)_{r_B} \\ (\underline{Q}_B^v)_{\theta_B} \\ (\underline{Q}_B^v)_{\eta_B} \end{bmatrix} , \tag{7.20}$$

where $\underline{m}_{ij}$ with $i, j, \in \theta, r, \eta$, are submatrices of $\underline{M}_B$, $\underline{Q}_B^e$ are the externally applied generalized forces, and $\underline{Q}_B^v$ are the quadratic velocity vectors resulting from the differentiation of the kinetic energy with respect to the body coordinates and with respect to time. These describe the gyroscopic and Coriolis force components [8, p. 221].

The equations of motion of the total system, as described by (7.1), can be obtained by combining the equations of motion of the individual n_B bodies, together with constraint equations of the Euler parameters and the kinematic constraints between the bodies. This system of equations can be systematically assembled from (7.20). For a complete derivation of these equations, a reference is made to [10, 14, 15].

7.2.1.3 Modal Reduction: Craig-Bampton

As described in Sect. 7.2.1.1, a modal representation of each flexible body is required to incorporate its non-rigid body dynamics in the equations of motion of the multibody system. By introducing modal deformation coordinates $\underline{\eta}$ instead of nodal displacements and rotations $\underline{u}$ in (7.8), the total number of generalized coordinates $\underline{q}$ required to describe the dynamics can be reduced. The challenge arises to select a set of modes that in a linear combination can accurately represent the local deformations of the body.

An often used reduction method is the one developed by Craig and Bampton [1]. Assuming that a lumped mass finite-element model and mesh are defined for the flexible body, the dynamic response of the undamped flexible body can be described by the differential equations

$$\underline{M}\,\ddot{\underline{u}}(t) + \underline{K}\underline{u}(t) = \underline{F}(t) \ , \tag{7.21}$$

where $\underline{M}$ and $\underline{K}$ are respectively the $(n_u \times n_u)$ mass and stiffness matrices, $\underline{F}$ is the $(n_u \times 1)$ column of applied loads, and $\underline{u}$ is a $(n_u \times 1)$ column with n_u displacement DOFs of the model.

In the applied Craig-Bampton method, the DOFs $\underline{u}$ are separated in n_{bo} boundary, or interface, DOFs $\underline{u}_b$ and n_{in} internal DOFs $\underline{u}_i$:

$$\underline{u} = \begin{bmatrix} \underline{u}_b \\ \underline{u}_i \end{bmatrix} . \tag{7.22}$$

The boundary DOFs are defined to be the DOFs that are connected to other bodies in the multibody simulation through joint or force elements.

Static constraint modes are used to exactly represent the static deformation of the body due to force elements and joint reaction forces at the boundary DOFs. After partitioning (7.21) according to (7.22), resulting in

$$\begin{bmatrix} \underline{M}_{bb} & \underline{M}_{bi} \\ \underline{M}_{ib} & \underline{M}_{ii} \end{bmatrix} \begin{bmatrix} \ddot{\underline{u}}_b \\ \ddot{\underline{u}}_i \end{bmatrix} + \begin{bmatrix} \underline{K}_{bb} & \underline{K}_{bi} \\ \underline{K}_{ib} & \underline{K}_{ii} \end{bmatrix} \begin{bmatrix} \underline{u}_b \\ \underline{u}_i \end{bmatrix} = \begin{bmatrix} \underline{F}_b \\ \underline{F}_i \end{bmatrix} , \tag{7.23}$$

the internal DOFs can be expressed as function of the boundary DOFs according to

$$\underline{u}_i = -\underline{K}_{ii}^{-1} \underline{K}_{ib} \underline{u}_b . \tag{7.24}$$

The static deformations, expressed as u^s, due to loads on the boundary DOFs can now be expressed in terms of the boundary DOFs $\underline{u}_b$ only

$$\underline{u}^s = \begin{bmatrix} \underline{u}_b \\ \underline{u}_i \end{bmatrix} = \begin{bmatrix} \underline{I}_{bb} \\ \underline{T}_{ib} \end{bmatrix} \underline{u}_b = \underline{T}_{nb} \underline{u}_b ; \qquad \underline{T}_{ib} = -\underline{K}_{ii}^{-1} \underline{K}_{ib} , \tag{7.25}$$

where $\underline{I}_{bb}$ represents the $(n_{bo} \times n_{bo})$ unity matrix. The n_{bo} columns of $\underline{T}_{nb}$ are referred to as the static constraint modes.

The static constraint modes are supplemented with fixed-interface normal modes. These modes are the eigenmodes as calculated from the undamped, free-vibrating body with all boundary DOFs constrained and can be obtained by solving the eigenvalue problem

$$\left[-\omega_j^2 \underline{M}_{ii} + \underline{K}_{ii} \right] \hat{\underline{\psi}}_j = \underline{0} , \qquad j = 1, 2, \ldots, n_{in} \tag{7.26}$$

where the resulting n_{in} angular eigenfrequencies and fixed-interface normal modes are stored in the matrices

$$\underline{\Omega}_{ii} = \begin{bmatrix} \omega_1 & & & \\ & \omega_2 & & \\ & & \ddots & \\ & & & \omega_{n_{in}} \end{bmatrix} , \qquad \underline{\Psi}_{ii} = \left[\hat{\underline{\psi}}_1 \; \hat{\underline{\psi}}_2 \; \hat{\underline{\psi}}_3 \; \cdots \; \hat{\underline{\psi}}_{n_{in}} \right] . \tag{7.27}$$

In order to sufficiently reduce the number of coordinates describing the deformation of the body, usually a limited set of normal modes $\hat{\underline{\psi}}_j$ is taken into account. The matrix containing the selected kept fixed-interface normal modes is indicated with $\underline{\Psi}_{ik}$. This subset of n_k kept normal modes is used to define the dynamic part of the deformation according to

$$\underline{u}^d = \begin{bmatrix} \underline{u}_b \\ \underline{u}_i \end{bmatrix} = \begin{bmatrix} \underline{O}_{bk} \\ \underline{\Psi}_{ik} \end{bmatrix} \underline{\zeta}_k \ , \tag{7.28}$$

where $\underline{O}_{bk}$ is the $(n_{bo} \times n_k)$ zero-matrix, corresponding to the fixed boundary DOFs, and $\underline{\zeta}_k$ are the modal coordinates corresponding to the kept fixed-interface normal modes.

Combining the static constraint modes and the kept fixed-interface normal modes, the deformation of the body is approximated by

$$\underline{u} = \underline{u}^s + \underline{u}^d = \begin{bmatrix} \underline{I}_{bb} \\ \underline{T}_{ib} \end{bmatrix} \underline{u}_b + \begin{bmatrix} \underline{O}_{bk} \\ \underline{\Psi}_{ik} \end{bmatrix} \underline{\zeta}_k = \begin{bmatrix} \underline{I}_{bb} & \underline{O}_{bk} \\ \underline{T}_{ib} & \underline{\Psi}_{ik} \end{bmatrix} \begin{bmatrix} \underline{u}_b \\ \underline{\zeta}_k \end{bmatrix} = \underline{\Psi}_{CB} \underline{\eta}_{CB} \ , \tag{7.29}$$

where $\underline{\eta}_{CB} = [\underline{u}_b^T \ \underline{\zeta}_k^T]^T$ and $\underline{\Psi}_{CB}$ is the Craig-Bampton reduction matrix. In order to obtain a significant reduction it is required that $n_{bo} + n_k \ll n_u$. By substituting (7.29) in (7.21) and premultiplying with $\underline{\Psi}_{CB}^T$, the equations of motion can be reduced to

$$\underline{M}^{CB} \ddot{\underline{\eta}}(t) + \underline{K}^{CB} \underline{\eta}(t) = \underline{F}^{CB}(t) \ , \tag{7.30}$$

where $\underline{M}^{CB} = \underline{\Psi}_{CB}^T \underline{M} \underline{\Psi}_{CB}$, $\underline{K}^{CB} = \underline{\Psi}_{CB}^T \underline{K} \underline{\Psi}_{CB}$, and $\underline{F}^{CB} = \underline{\Psi}_{CB}^T \underline{F}$.

The eigenmodes of (7.30) are orthogonalized with respect to $\underline{M}^{CB}$ and $\underline{K}^{CB}$ before integrating them in the equations of motion of the multibody system [10]. This both improves the numerical performance of multibody solver and enables the identification of possible rigid body modes, which are to be excluded from the set of modal coordinates, since the rigid body motion in the multibody formulation is already defined by the reference coordinates $\underline{r}_B$ and $\underline{\theta}_B$.

In order to obtain the orthogonalized mode set, the generalized eigenvalue problem

$$[-\hat{\omega}_j^2 \underline{M}^{CB} + \underline{K}^{CB}] \underline{\xi}_j = \underline{0}, \qquad j = 1, 2, \ldots, (n_{bo} + n_k) \ , \tag{7.31}$$

is solved, where $\hat{\omega}_j$ are the undamped angular eigenfrequencies and $\underline{\xi}_j$ the corresponding eigenvectors. The eigenvectors are gathered in the columns of the matrix

$$\underline{\Xi} = \begin{bmatrix} \underline{\Xi}_{rb} & \underline{\Xi}_{fl} \end{bmatrix} \ , \tag{7.32}$$

which is partitioned in possible rigid body modes $\underline{\Xi}_{rb}$ and the flexible modes $\underline{\Xi}_{fl}$. The rigid body modes are identified by their eigenfrequencies $\hat{\omega}_j$ being (almost) zero. To avoid a redundant description of the rigid body modes in the multibody formulation, the set $\underline{\Xi}_{rb}$ is not used. The modes $\underline{\Xi}_{fl}$ linearly transform the modes $\underline{\Psi}_{CB}$ into the new, orthogonalized mode set

$$\underline{\Psi} = \underline{\Psi}_{CB} \underline{\Xi}_{fl} \ , \tag{7.33}$$

which is used in the multibody formulation and couples the final generalized DOFs $\underline{\eta}$ to the original set of physical DOFs $\underline{u}$ according to

$$\underline{u} = \underline{\Psi}\underline{\eta} \,. \tag{7.34}$$

The final reduced version of (7.21) becomes

$$\underline{\Psi}^T \underline{M}\,\underline{\Psi}\ddot{\underline{\eta}} + \underline{\Psi}^T \underline{K}\,\underline{\Psi}\dot{\underline{\eta}} = \underline{\Psi}^T \underline{F} \,, \tag{7.35}$$

where $\underline{\Psi}^T \underline{K}\,\underline{\Psi} = K^{red}$ is the reduced stiffness matrix and $\underline{\Psi}^T \underline{M}\,\underline{\Psi} = \underline{m}_{\eta\eta}$ is the component of the mass matrix corresponding to the modal coordinates in (7.20).

7.2.2 *Tire Dynamics*

Tire dynamics form an essential part in accurately describing the wheel shimmy phenomenon. A tire model, featured in the Virtual.Lab software [10], describes the dynamics between the tire body and the runway. Based on the position and velocity of the tire with respect to the runway, the resulting normal force F_n, lateral force F_y, longitudinal force F_x, and self-aligning moment around the vertical axis M_z from the road to the tire are determined.

Of these forces, F_y and M_z have the largest influence on the shimmy oscillations, because the oscillations are characterized most by lateral and yaw motion of the tire. The lateral force F_y is a function of the side slip angle α. This angle is defined as the acute angle between the longitudinal tire direction, associated with a longitudinal velocity vector $\vec{V}_x$, and the velocity vector $\vec{V}_{BP}$ of the bottom point of the tire. These vectors are visualised in Fig. 7.3a. The side slip angle is calculated as

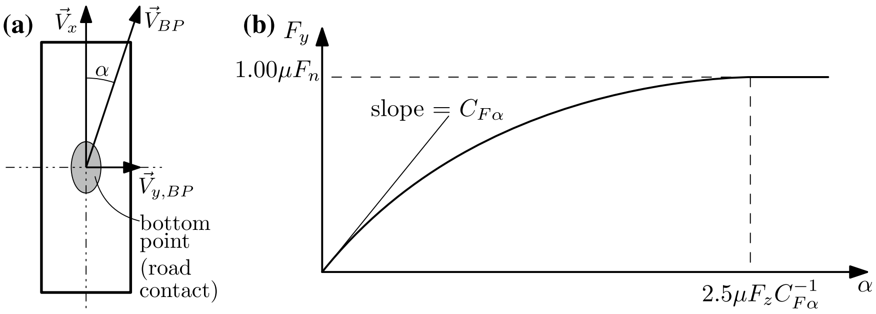

Fig. 7.3 **a** Top view of a tire with velocity and side slip angle definitions. **b** Tire lateral force as function of the side slip angle [10]

$$\alpha = \tan^{-1}\left(\frac{|\vec{V}_{y,BP}|}{|\vec{V}_x|}\right) . \tag{7.36}$$

The instantaneous lateral force F_y is defined as a third-order polynomial function of α for $0 < \alpha < 2.5\mu F_n C_{F\alpha}^{-1}$ [10], as shown in Fig. 7.3b. The boundary conditions of $F_y(\alpha)$ are defined as

$$F_y(0) = 0; \quad \frac{dF_y}{d\alpha}(0) = C_{F\alpha}; \quad F_y(2.5\mu F_n C_{F\alpha}^{-1}) = \mu F_n; \quad \frac{dF_y}{d\alpha}(2.5\mu F_n C_{F\alpha}^{-1}) = 0 , \tag{7.37}$$

where $C_{F\alpha}$ is a user-supplied constant indicating the cornering stiffness of the tire and μ is the static friction coefficient between the tire and the road. For small slip angles, this cornering stiffness dictates the lateral force characteristic of the tire. For larger slip angles, the force F_y reaches a maximum of μF_n and stays constant for $\alpha > 2.5\mu F_n C_{F\alpha}^{-1}$.

In reality, the lateral force does not act exactly on the bottom point of the tire, but rather just behind it. Therefore, the self-aligning moment is introduced and defined by

$$M_z = -r_p F_y , \tag{7.38}$$

where r_p is the pneumatic trail, which is assumed to be constant.

7.2.2.1 Relaxation Behavior

The response of the lateral force to side slip is not instantaneous. There is a phase lag between the side slip angle α and the developed lateral force F_y. This relaxation behavior of the tire is characterised by the relaxation length σ. This is the distance a tire has to roll in order to generate 63% of the steady-state lateral force, assuming α is constant.

In this particular tire model, the relaxation behavior of the tire is modeled by introducing a relaxation time t_σ for the lateral force and self-aligning moment:

$$\dot{\tilde{F}}_y = \frac{1}{t_\sigma}\left(F_y - \tilde{F}_y\right) , \quad \dot{\tilde{M}}_z = \frac{1}{t_\sigma}\left(M_z - \tilde{M}_z\right) , \tag{7.39}$$

where the relaxation time is derived from the relaxation length according to

$$t_\sigma = \frac{\sigma}{|\vec{V}_x|} . \tag{7.40}$$

In (7.39), $\tilde{F}_y$ and $\tilde{M}_z$ are the lateral force and self-aligning moment that include the relaxation behavior. The two differential equations in (7.39) are added to the system of DAE that are analysed by the Motion solver. Therefore, $\tilde{F}_y$ and $\tilde{M}_z$ appear as additional states $\underline{\chi}$ in (7.3).

Before the calculated forces and moments (F_n, F_x, $\tilde{F}_y$, and $\tilde{M}_z$) are applied to the tire body in the multibody system, the friction limit is taken into account. This implies that the vector sum of the lateral and longitudinal forces is reduced in case it exceeds the maximum friction force generated by the tire, according to

$$\sqrt{F_x^2 + \tilde{F}_y^2} \leq \mu F_n \; . \tag{7.41}$$

7.3 Multibody Model of a Nose Landing Gear

A dedicated multibody model is created to conduct a shimmy study. This model is referred to as the 'bifurcation study model', or simply the 'study model'. The functionalities of a parameterized CAD model of a landing gear, supplied by Fokker LG, are employed to generate the CAD geometry of the multibody study model. The study model contains many of the complexities that are normally present in multibody landing gear models used in the landing gear industry.

7.3.1 Landing Gear Model for Bifurcation Study

A side view of the study model is shown in Fig. 7.4. The figure shows the landing gear structure, the runway, and the airframe. Global coordinate directions are included in all figures. Standard aircraft industry coordinate definitions are used, with the x-axis directed rearward in the longitudinal direction and the z-axis directed vertically upwards.

The airframe, which is represented by dashed lines, is a rigid frame representing the fuselage of the aircraft to which the landing gear is attached. It has a mass that induces the nominal vertical force on the landing gear structure. The airframe is constrained to move only vertically with respect to the fixed global axis system, so

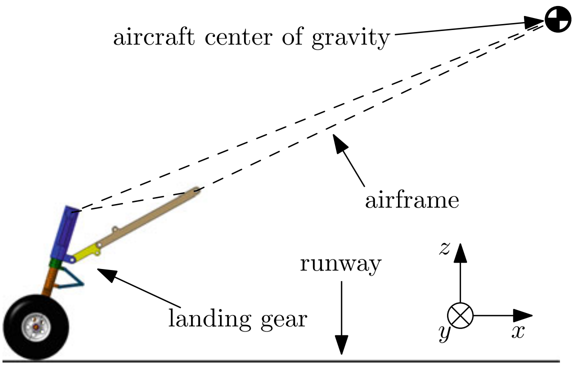

Fig. 7.4 Side view of the study model

Fig. 7.5 Isometric view of the rear side of the study model, including the names of the individual bodies

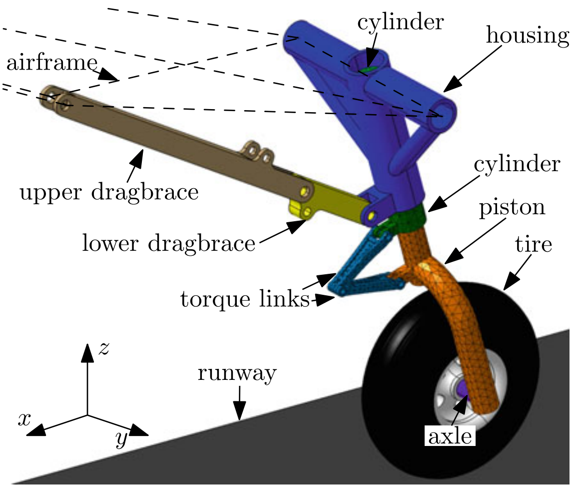

the landing gear can drop down onto the runway. The runway is moved backwards relative to the landing gear to simulate a forward motion of the aircraft.

A more detailed, isometric view of the landing gear is shown in Fig. 7.5. All bodies are colored separately and their names are indicated using labels. Again, the airframe is represented by dashed lines. Connected to the airframe are the housing and the upper drag brace. The two are connected through the lower drag brace. These three rigid bodies are constrained such that these cannot move with respect to the airframe or to each other. Therefore, the airframe, upper- and lower drag brace, and the housing move as one rigid body. The bodies are constrained in a statically determined way, as to not introduce any redundant constraints.

The housing takes up a cylindrical part named the cylinder. Between these two bodies, only rotation about their co-axial axis is allowed. During taxiing, this DOF enables the steering of the nose landing gear. During landing or take off, the steering actuator is turned off. In that case, hydraulic shimmy damping is supplied to this DOF by the same actuator. A quadratic damping curve is used to model the hydraulic damping. The used nonlinear relation for the damping moment is displayed in Fig. 7.6a, and is similar to the characteristics of a shimmy damper used in the industry. In case the steering actuator is turned on, linear rotational stiffness and damping are applied on this DOF instead.

The piston can move axially with respect to the cylinder, as well as rotate about their co-axial axis. In reality, this motion is enabled by two bearings that guide the sliding and rotating motion of the piston with respect to the cylinder. In the multibody model, flexible-point-curve-joint constraints [10] are used to simulate these bearings and constrain the two flexible bodies together. This particular landing gear has an asymmetric piston, with a half-forked design, see Fig. 7.5. The piston also forms the bottom of the shock absorber. A vertical shock absorber force acts between the cylinder and the piston. The static shock absorber force is modeled by a non-linear,

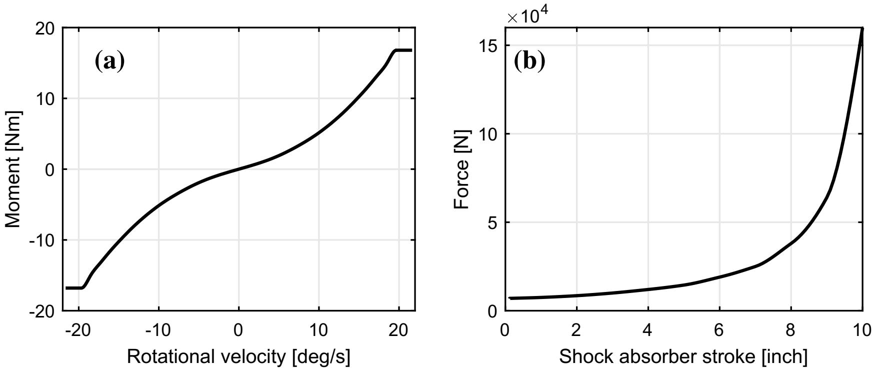

Fig. 7.6 **a** Nonlinear damping moment curve of the shimmy damper. **b** Nonlinear shock absorber force

progressive spring, closely resembling the static shock absorber forces as experienced in industry models. The force is detailed as a function of shock absorber stroke in Fig. 7.6b.

The torque links are two bars that are hinged together. These restrict the rotation of the piston relative to the cylinder, without constraining the shock absorber stroke. Therefore, the torque links determine to a large extent the yaw-stiffness of the landing gear structure. The design of the two torque links is identical.

A rigid axle connects the tire to the piston. The tire is simulated by a rigid body, which is only used to characterize the tire mass and rotational inertia. The forces exerted on the tire by the runway are calculated using the tire model described in Sect. 7.2.2. This model is featured in the Virtual.Lab Motion software and is also used in the landing gear industry.

7.3.1.1 Structural Flexibility—Modal Reduction

For the bodies described in Sect. 7.3.1, the structural compliance of the cylinder, the piston, and the two torque links is taken into account. By default, the Virtual.Lab software only supports Component Mode Synthesis (CMS) as a method to model the flexibility of bodies. Therefore, Craig-Bampton mode sets are used. To this end, a finite element mesh is created for each body, and the interface DOFs are determined, based on the joints and actuators attached to each body. According to the theory described in Sect. 7.2.1.3, static constraint modes are determined for each body, along with fixed-interface normal modes. Material properties of steel are used for all flexible bodies, with a mass density of $7860\,\text{kg/m}^3$, a Young's modulus of $2 \times 10^{11}\,\text{N/m}^2$, and a Poisson ratio of 0.226.

Due to the various joints and force-elements connected to the flexible bodies, 53 static constraint modes are required to represent the static stiffness of the four flexible bodies: 10 for each torque link, 18 for the piston, and 15 for the cylinder. In order to reduce the model complexity sufficiently to stay within the limitations of the simulation framework, no normal modes are included in the mode sets for the flexible bodies: i.e., $n_k = 0$, in (7.28). Therefore, the total number of modal coordinates $n_{\underline{\eta}}$ is given by the number of static constraint modes minus the 4×6 rigid body modes. This results in 29 modal coordinates.

In order to verify whether the applied reduction has a significant effect on the dynamics of the system, the reduced study model is compared to an unreduced model. As use of CMS is required, a model with larger Craig-Bampton mode sets is assumed to approximate the unreduced model sufficiently accurately. For this 'unreduced' model, Craig-Bampton mode sets with $n_k = 10$ kept fixed-interface normal modes per flexible body are used.

The eigenfrequencies and dimensionless damping ratios of the two linearized landing gear models are compared. A simulation is performed on each of the models, where the landing gear is suspended stationary in the air, without tire-road contact. The shock absorber stroke is fixed at 5 in., which is midway between fully compressed and fully extended. By computing the linearized system matrix in this equilibrium situation, the eigenmodes, eigenfrequencies, and dimensionless damping ratios can be determined. The latter two quantities are calculated from the eigenvalues of the system λ_i, according to $\omega_{u,i} = \sqrt{Re(\lambda_i)^2 + Im(\lambda_i)^2}$, where $\omega_{u,i}$ indicates the i^{th} undamped angular eigenfrequency, and $\zeta_i = \frac{-Re(\lambda_i)}{\omega_{u,i}}$, where ζ_i is the corresponding dimensionless damping ratio. Even though the multibody system is generally viscously damped, the dimensionless damping ratios (which in principle only can be used in the proportionally damped case) characterize the damping of the modes, assuming these are only weakly damped. The lowest six eigenfrequencies of both models, including damping factors, are listed in Table 7.1. Visualisations of these eigenmodes are shown in Fig. 7.7a, b.

The results show that there are 2 rigid body modes present in the model, if there is no tire road contact. These are the unobstructed rotation of the tire body and the yaw motion of the entire 'tire-axle-piston-torque links-cylinder' sub-structure with respect to the housing. The latter is caused by the steering DOF between the cylinder

Table 7.1 The lowest six eigenfrequencies and the corresponding damping factors of the unreduced study model and the reduced study model

Mode shape	Unreduced study model		Reduced study model	
	ω_u (Hz)	ζ (–)	ω_u (Hz)	ζ (–)
Rigid body wheel	0.01		0.03	
Rigid body yaw	0.02		0.03	
Longitudinal bending	43.0	0.037	46.5	0.034
Lateral bending	47.0	0.038	47.0	0.038
Yaw, torsional	95.8	0.10	95.8	0.10
Lateral bending (2nd)	179.2	0.059	178.8	0.061
...	>300	...	>300	...

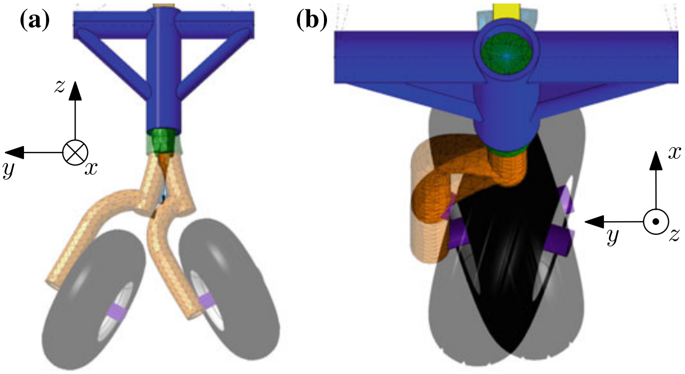

Fig. 7.7 **a** Visualisation of the first lateral bending mode of the study model. **b** Visualisation of the first torsional mode of the study model

and the housing, because the steering actuator, when turned off, does not include any stiffness.

The two most relevant eigenmodes for the shimmy phenomenon are the first lateral bending mode and the first torsional mode. The results show that these remain virtually unchanged by the modal reduction. There is a notable difference in the eigenfrequency of the longitudinal bending mode: roughly 8% between the reduced and the unreduced model. However, in a single-wheeled landing gear, such as presented here, the longitudinal structural dynamics have a relatively small effect on shimmy. Therefore, it can be concluded that the applied modal reduction is sufficiently accurate for the purpose of a shimmy analysis.

7.3.1.2 Model Dimension of the Study Model

The total multibody model contains 16 bodies. These also include weightless dummy-bodies that do not affect the dynamics and are mostly used for modeling convenience. The rigid body motion of all the bodies is described by $7 \times 16 = 112$ generalized coordinates. Furthermore, the structural flexibility of four of the bodies is described by 29 modal coordinates in total, as described in Sect. 7.3.1.1. Each of the two flexible-point-curve-joints introduces 1 dependent generalized coordinate. Lastly, for the Motion solver, torsional springs introduce additional redundant generalized coordinates, which represent the rotational displacement of the respective spring. There are 3 of these torsional springs present in the model, bringing the total count to 146 generalized coordinates in $\underline{q}$.

Together with the 16 Euler parameter constraints, the joints and drivers in the model introduce a total of 114 constraint equations. By subtracting this number from the total number of generalized coordinates, the total number of independent generalized coordinates can be determined, which is 32. Therefore, the total first

Fig. 7.8 Calculation resulting in the number of independent states in the first-order equation of motion (7.3) for the study model

Bodies	$16 \times 7 =$	112	
Modal coordinates	$4 + 4 + 12 + 9 =$	29	
flex-point-curve-joints	$2 \times 1 =$	2	
Torsional springs	$3 \times 1 =$	3	+
Generalized coordinates in $\underline{q}$		**146**	
Euler parameter constraints	$16 \times 1 =$	16	
Joint/driver constraints		98	−
Indep. generalized coord. $\underline{q}_I$		**32**	×2
Indep. states $\underline{x}_I$		**64**	
Tire states $\underline{\chi}$		2	+
Independent states in (3)		**66**	

order representation of the equations of motion, as described by (7.3), contains 66 independent states, as there are also two tire states $\underline{\chi}$ added, as described in Sect. 7.2.2.1. This calculation is summarized in Fig. 7.8.

7.3.2 Comparison to an Industry Model

The study model, as presented above, is based on the nose landing gear of a typical fighter aircraft. In order to verify if the dynamic behavior of the study model is indeed realistic for such a landing gear, it is compared to the dynamic behavior of the original multibody model made by Fokker Landing Gear, which represents a nose landing gear of a typical fighter aircraft. The latter model is referred to as the 'industry model'.

7.3.2.1 The Industry Model

Before the two models are compared, the industry model is simplified to a certain extent, to ensure that both models include the same dynamic effects. This implies that the following features are removed from the industry model before analysis:

- The **airframe stiffness** is normally taken into account in Fokker models. For purposes of this study, the airframe stiffness is removed from the industry model and the assumption is made that the airframe is completely rigid.
- Standard multibody models from Fokker include **free-play**. This can for instance be lateral free-play between the landing gear structure and the airframe, as well as free-play in the torque links, which affects the yaw motion of the tire. These types of free-play can result in small-amplitude limit cycle oscillations of the landing

gear at all forward velocities. These are too small to be considered as shimmy, but are periodic solutions of the system nonetheless. Even though continuation of periodic solutions is possible using AUTO, it is computationally more expensive than continuation of (quasi-)static solutions and is not considered here. Therefore, the free-play is not taken into consideration and is removed from the industry model. All the connections that are originally governed by free-play are considered close fits.

- In the original Fokker model, the rotational **friction** of the bearings between the piston and the cylinder is taken into account. In the industry model discussed here, all friction is neglected. In a shimmy analysis, friction tends to hide shimmy behavior, as it dissipates energy from the system. Therefore, neglecting friction can be considered to be a worst-case assumption with respect to the emergence of shimmy.

These simplifications imply that the dynamic behavior of the model indicated here as ‘industry model’ will be slightly different from those used in reality. However, the main effects that influence shimmy behavior, such as the tire dynamics and viscous shimmy damper properties, remain unchanged.

Even though the industry model is simplified to some extent, it still exceeds the study model in terms of complexity. In this case, the industry model contains 26 bodies, of which 6 bodies are flexible. This results in an industry model having more than 400 independent states in the first-order form of the equations of motion. As a model of this size still imposes computational challenges for the current bifurcation analysis framework, the study model, with 66 independent states, is used to conduct the bifurcation analysis.

7.3.2.2 Structural Compliance Comparison

Since both models now contain the same dynamic effects, a comparison is pursued. The comparison focuses on the dynamic properties of the landing gear structure, because these are influenced most by the geometry of the bodies, which is slightly different for both models.

The static stiffness is determined by performing time-simulations of both models where a unit force/moment is applied to the axle, in a situation where the airframe is fixed in space while there is no tire-road contact. For this particular analysis, the rotation between the piston and the cylinder is suppressed. The resulting lateral stiffness and yaw stiffness of the landing gear are shown in Fig. 7.9a and Fig. 7.9b, respectively. These are known to have the largest influence on the shimmy behavior compared to stiffnesses in other directions.

Figure 7.9a, b show the stiffness as function of the shock absorber stroke, where 0 in. corresponds to a fully extended shock absorber and 10 in. to a fully compressed shock absorber. In both models, the stiffness increases with increasing shock absorber stroke. In the lateral direction, as seen in Fig. 7.9a, this increase can partially be explained by the fact that the arm at which the lateral force acts on the structure

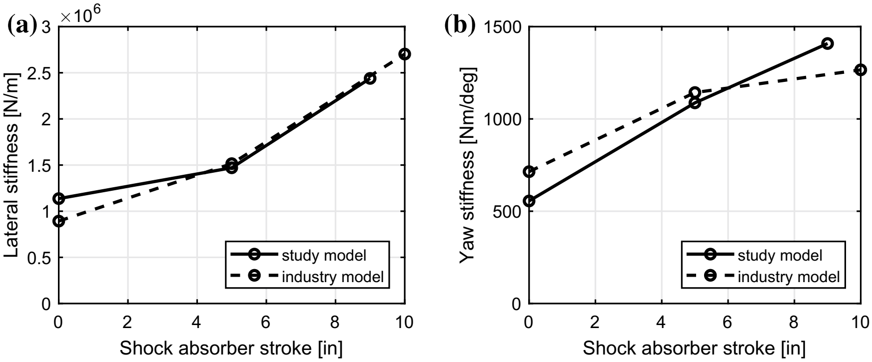

Fig. 7.9 **a** Lateral stiffness of the landing gear structure of the study model, compared to the industry model. **b** Yaw stiffness of the landing gear structure of the study model, compared to the industry model

is a function of the shock absorber stroke. Secondly, a larger part of the piston is inserted in the cylinder if the shock absorber is compressed, thereby also increasing the lateral stiffness. In the yaw direction, shown in Fig. 7.9b, the stiffness is affected the most by the relative angle of the two torque links, which directly depends on the shock absorber stroke. This greatly effects the yaw stiffness.

When comparing the structural stiffness of the two models, it can be seen that both models are in agreement, even though the study model contains less flexible components. It can thus be concluded that the four flexible components of the study model approximate the compliance of much larger industry model accurately.

7.3.2.3 Eigenvalue Analysis

The study model and the industry model are also compared by analyzing eigenfrequencies and modal damping factors of the linearized systems. The same method as described in Sect. 7.3.1.1 is employed: the system is linearized around a static equilibrium situation, where there is no tire-road contact. The relevant resulting eigenfrequencies, and modal damping factors of the two models are shown in Table 7.2.

The results show that the eigenfrequencies of both models are largely in accordance. Most relevant are the eigenfrequencies of the lateral bending mode and the torsional mode in the yaw direction. The lateral bending eigenfrequency compares well, as there is only 2% difference between the eigenfrequencies. The difference between the eigenfrequencies in the yaw direction is with 12% slightly larger. This might be caused by a different mass distribution between the two models.

Furthermore, the damping factors of the lateral and longitudinal modes differ by roughly one order of magnitude between the models. This might be a consequence of the additional flexible bodies in the industry model. The damping factor in yaw-direction is in accordance.

Table 7.2 Relevant Eigenfrequencies and damping factors of the study model and the industry model

Mode shape	Study model		Industry model	
	ω_u (Hz)	ζ (–)	ω_u (Hz)	ζ (–)
Longitudinal bending	46.5	0.034	47.6	0.0025
Lateral bending	47.0	0.038	46.1	0.0035
Yaw, torsional	95.8	0.10	109.4	0.099

7.4 Continuation Analysis of a Multibody System

A recently developed simulation framework by Tartaruga et al. [11] is adapted to perform 1-parameter bifurcation analyses on the study model as described in Sect. 7.3.1. The continuation software AUTO [5] is coupled to the Virtual.Lab Motion multibody solver through MATLAB. A custom version of the Motion solver is used that includes a MATLAB interface. This interface makes all the states $\underline{x}$ of the first-order equations of motion, (7.3), and the bifurcation parameters of a model available in the MATLAB-workspace.

The bifurcation analysis has to be started from a (quasi-)static stable equilibrium solution of the system. This solution is obtained by integrating the equations of motion, (7.3), in time, from an initial configuration, until the transient dynamics have damped out and the time derivatives of all states are below a small tolerance value. The solution is then assumed to be close enough to the final (quasi-)static solution and the values of all the independent states are stored for use in the next step of the analysis.

From this initial solution, the challenge is to find subsequent (quasi-)static solutions for varying values of the bifurcation parameter. For this, the Dynamical Systems Toolbox (DST) is employed [3]. The DST is an open source MATLAB-toolbox that encapsulates all the functionalities of the bifurcation software AUTO. The original FORTRAN-code of AUTO is integrated in the toolbox via 'MATLAB-executable'-files, or MEX-files. The toolbox is normally used to compute branches of solutions of analytical nonlinear systems by evaluating the time derivatives of the states as function of the states and a bifurcation parameter p, according to

$$\underline{\dot{y}} = f\left(\underline{y}, p\right) \ . \tag{7.42}$$

By coupling the DST to the Motion solver and performing a co-simulation, one can impose that $\underline{y} = \{\underline{x}_I, \underline{\chi}\}$, and the multibody system can be evaluated by the DST using the same techniques. This co-simulation workflow is visualised in Fig. 7.10.

Figure 7.10 shows that, given a viable set of inputs $\{\underline{x}_I, \underline{\chi}, p\}$, the Motion solver is able to algebraically solve the first-order equations of motion, (7.3), which results in the time derivatives of the states: $\underline{\dot{x}}_I$ and $\underline{\dot{\chi}}$. These are used by the DST, and the underlying AUTO software, to identify (quasi-)static solutions, stability properties

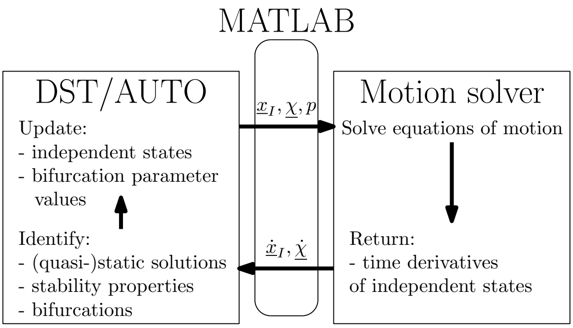

Fig. 7.10 Schematic of the coupling between the dynamical systems toolbox (DST) and the motion solver through MATLAB

and bifurcation points. This is an iterative process, where the DST constantly updates and applies perturbations the states of the model.

During this continuation analysis, the stability properties of the solutions are determined by analyzing the eigenvalues of the system Jacobian around the solution, which is determined through a finite-difference method. These eigenvalues are also used to detect possible Hopf bifurcations, which are defined by a complex conjugate pair of eigenvalues transversely crossing the imaginary axis [12, pp. 200–201]. By monitoring the number of eigenvalues of the Jacobian in the left-half complex plane together with the real part of the eigenvalue closest to the imaginary axis [4], the AUTO software can detect and locate Hopf bifurcations.

The operation of the simulation framework is discussed in more detail in [2]. Furthermore, as described in [11], this simulation framework also allows for the continuation of periodic solutions of small multibody systems. However, because this requires increasing computational effort for larger models, these type of analyses are not considered here.

7.5 Landing Gear Shimmy Analysis Using Bifurcation Methods

The simulation framework presented in Sect. 7.4 is used to analyse the possible occurrence of shimmy in the flexible landing gear multibody model presented in Sect. 7.3. The relevant (and safety critical) case of a leaking shimmy damper is considered. To emulate the loss of damping in the shimmy damper, the damping moment curve, applied by the hydraulic shimmy damper and shown in Fig. 7.6a, is reduced by a factor d_{damper}. Initially d_{damper} is chosen to be 0.03. This corresponds to a damping moment of only 3% of the original value. As will be shown, this will lead to shimmy within the operational parameter space.

A 1-parameter bifurcation analysis is performed on the landing gear model. The relative velocity of the runway with respect to the landing gear V is chosen to be the primary bifurcation parameter as the velocity has a large influence on the occurrence

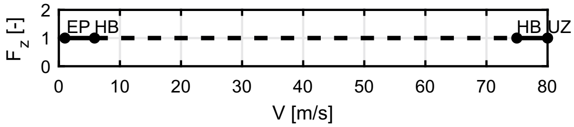

Fig. 7.11 1-Parameter bifurcation diagram. 'EP' and 'UZ' indicate the start and end of the solution branch respectively. HB indicates a supercritical Hopf bifurcation

Fig. 7.12 Eigenvalues of the system Jacobian for the solutions presented in Fig. 7.11. Arrows indicate the trace of the eigenvalues for increasing velocity V. Only the eigenvalues closest to the imaginary axis are shown. The critical eigenvalue pairs are indicated with larger dots

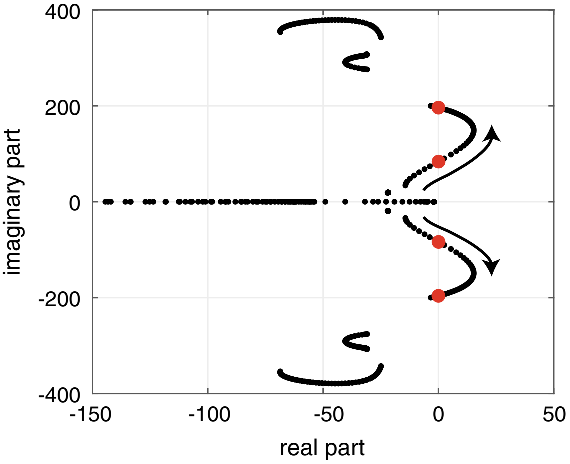

of shimmy and it can vary significantly during landing and take-off events. The result of this 1-parameter bifurcation analysis is shown in Fig. 7.11. Solid lines indicate (quasi-)static *stable* solutions, while dashed lines indicate (quasi-)static *unstable* solutions.

The figure shows the bifurcation diagram as function of the velocity, at a constant vertical force F_z. The vertical force is normalized at 20 kN. The continuation analysis is started at a velocity of $V = 1$ m/s. This (quasi-)static starting solution, which is determined using conventional time simulation, is marked with 'EP'. From this point, the (quasi-)static solution is continued for increasing velocities up to 80 m/s, where the end point of the branch is marked by 'UZ'. This is the maximum landing/take-off velocity for this type of landing gear. Along the solution branch, two supercritical Hopf bifurcations are encountered at 5.8 and 75 m/s, both marked by 'HB'. These indicate the edges of a domain where the stationary (quasi-)static solution becomes unstable and a coexisting stable oscillatory solution emerges. This is the velocity range where the landing gear model shows shimmy.

The eigenvalues of the system Jacobian are presented in Fig. 7.12 as function of the landing gear velocity V. The results show that as the velocity V changes, the system dynamics, and thus the eigenvalues of the linearized system, change. One pair of complex conjugate eigenvalues can be observed crossing the imaginary axis to the right-half complex plain and back again. These two crossings represent the

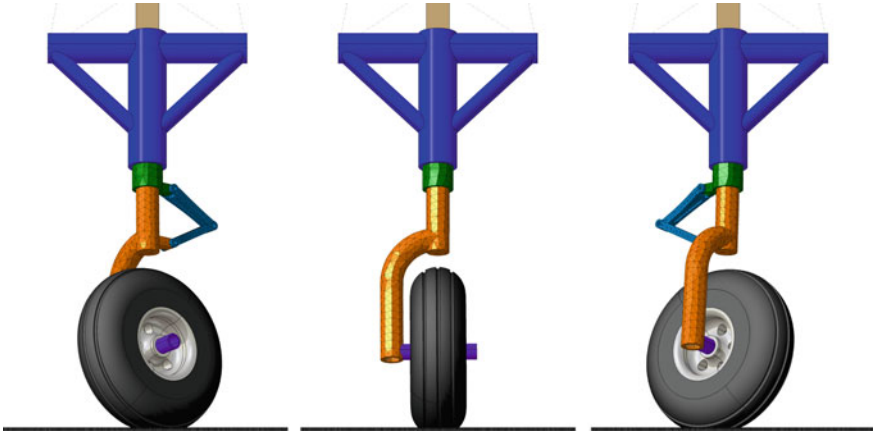

Fig. 7.13 The equilibrium solution at the Hopf bifurcation of $V = 5.8\,\text{m/s}$ (center) and the visualisation of the eigenmode corresponding to the critical eigenvalue pair (left and right)

Hopf-bifuractions at $V = 5.8\,\text{m/s}$ and $V = 75\,\text{m/s}$, respectively, and are marked by larger dots in the figure.

The eigenvectors of the linearized system corresponding to the critical eigenvalue pair can be visualized. The center figure of Fig. 7.13 shows the equilibrium solution of the system at the Hopf bifurcation of $V = 5.8\,\text{m/s}$. Adding or subtracting the real part of the critical eigenvector, which is dominant compared to the negligibly small imaginary part, to this equilibrium solution results in the visualisations shown on the left and right side of Fig. 7.13, respectively. These figures therefore indicate the shape of the landing gear corresponding to the initial oscillation that originates from the Hopf bifurcation. Figure 7.13 shows that the discrete steering DOF, where the shimmy damper acts, is dominant in the oscillating motion. Furthermore, the lateral bending of the piston also plays a significant role.

The (quasi-)static equilibrium solutions of the branch can further be analysed as a function of the bifurcation parameter V. Figure 7.14a, b show the yaw angle and lateral position of the tire as a function of the runway velocity, respectively. The tire has a static yaw angle deflection to the right, due to the asymmetric design of the piston. This static yaw angle is smaller at higher velocities. Figure 7.14b shows that the tire has a small, roughly constant lateral deflection, enabled by the compliance of the flexible piston. The unstable (quasi-)static solutions shown here cannot be determined using time simulation, as these will diverge to a co-existing limit cycle oscillation.

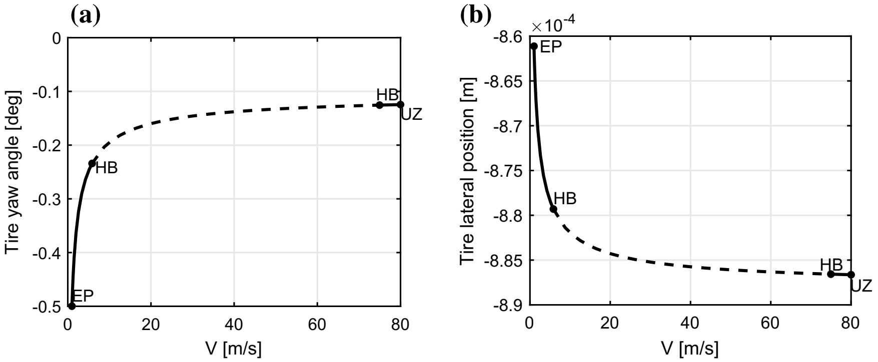

Fig. 7.14 **a** The tire yaw angle of the equilibrium solutions, as function of the bifurcation parameter V at $F_z(norm.) = 1$. Solid lines are stable solutions, while dashed lines are unstable. **b** The tire lateral position of the equilibrium solutions, as function of the bifurcation parameter V at $F_z(norm.) = 1$. Solid lines are stable solutions, while dashed lines are unstable

7.5.1 Quasi-2-Parameter Bifurcation Diagrams

The 1-parameter bifurcation analysis can be repeated for different values of the normal force on the landing gear F_z. By doing so, the stability of the landing gear is evaluated in the 2-parameter space (V, F_z). The results of this quasi-2-parameter bifurcation study are visualized in Fig. 7.15a. Individual 1-parameter bifurcation analyses show the stability of the equilibrium solutions at constant values for F_z. By connecting the Hopf bifurcation points for multiple values of F_z, the stability boundary in the 2-parameter plane can be visualised, as indicated by the black line in Fig. 7.15b. In this figure, the unstable parameter domain is shaded.

The results of the bifurcation analysis are verified through a comparison with standard time simulations of the same multibody model. An aircraft landing is simulated by gradually lowering the landing gear on the moving runway under the influence of gravity and the applied vertical force F_z. After the transient behavior has dampened out, the stability properties of the steady-state solution of the model are assessed. This process is repeated for various parameters V and F_z. The results are shown in Fig. 7.15b with black letters, indicating a stable (quasi-)static solution with ‘s’ and an unstable solution with ‘u’. In case of the marker ‘m’, the solution is considered to be marginally stable, as small limit cycle oscillations were found that may only damp out for very long simulation times.

The comparison with 30 of these conventional time-simulations, as displayed in Fig. 7.15b, reveals that the two methods are in accordance. Furthermore, for the results shown here, both methods require a similar amount of computational time. However, the grid of found solutions in the (V, F_z)-parameter space of the bifurcation analysis is much denser and even reveals the exact location of 20 Hopf points on the stability boundary. Achieving the same kind of accuracy with the conventional

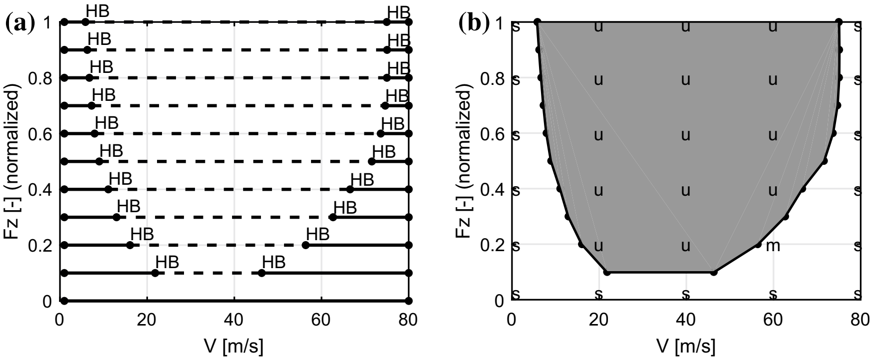

Fig. 7.15 **a** Results of multiple 1-parameter bifurcation analyses, where 'HB' indicates the supercritical Hopf bifurcations. Solid lines indicate locally stable solutions, while dashed lines mark local instability of the (quasi-)static solutions. **b** The same stability boundary as in Fig. 7.15a is indicated by a black line and the results of 30 time-domain simulations are indicated by markers: 's' is stable, 'u' is unstable, and 'm' is marginally stable. The unstable domain is colored gray

time-simulation method would require a multiplication of the performed simulations, and thus of the computational time needed.

When studying the shape of the unstable domain as displayed in Fig. 7.15b, it can be recognized that the range of unstable velocities is smaller at lower vertical loads. The results in Sect. 7.3.2.2 already showed that the lateral and yaw stiffness of the landing gear structure are significantly lower in this region, because the shock absorber is extended. Additionally, tire dynamics will be affected by the decreased vertical force, lowering the ability of the tire to generate lateral force, resulting in less shimmy. Probably, both these effects are responsible for the variation in shimmy behavior as function of the vertical load.

7.5.2 Sensitivity Studies

Using the bifurcation analysis framework, sensitivity studies are performed on the study model. Several design parameters, that are known to have a large influence on the shimmy behavior of the landing gear, are varied and their influence is quantified by generating new quasi-2-parameter bifurcation diagrams, with F_z and V as the bifurcation parameters. Design parameters of interest are the previously discussed reduction factor for the shimmy damper d_{damper}, the mechanical trail, and the steering stiffness.

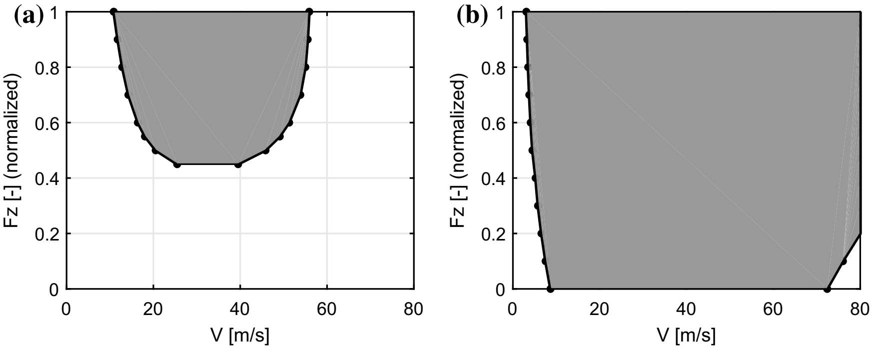

Fig. 7.16 **a** Unstable domain in the (V, F_z)-parameter space for $d_{damper} = 0.04$. The unstable domain is colored gray. **b** Unstable domain in the (V, F_z)-parameter space for $d_{damper} = 0.02$. The unstable domain is colored gray

7.5.2.1 Shimmy Damping Sensitivity Study

The effects of changing the reduction factor d_{damper} of the shimmy damper moment curve are investigated first. The stability boundary is determined using the bifurcation analysis framework, for various values of d_{damper}. The landing gear is found to be stable over the entire considered parameter space, in case $d_{damper} = 1$. From there on, the damping factor is gradually decreased to determine how much shimmy damper malfunction is required for the landing gear stability to be severely compromised.

Results show that even for a reduction factor of $d_{damper} = 0.05$ this landing gear is stable over the entire considered (V, F_z)-space. However, when the damping coefficient of the shimmy damper is reduced further, to $d_{damper} = 0.04$, there emerges an unstable domain for higher vertical loads, as shown in Fig. 7.16a. Further reduction of the damping properties to $d_{damper} = 0.03$, leads to the increase of the size of this unstable domain, as was already shown in Fig. 7.15b. Eventually, when the shimmy damper force is reduced to only 2% of its original value, almost all equilibrium solutions in the operational parameter space are unstable, as is displayed in Fig. 7.16b. In this situation, the shimmy damper is no longer strong enough to prevent shimmy oscillations.

From these results, it can be concluded that the shimmy damper has a significant effect on the stability of the landing gear. Proper damping in the yaw direction is essential to prevent shimmy. Furthermore, it is shown that only after severe failure, i.e., leakage, of the shimmy damper, below $d_{damper} = 0.05$, will shimmy occur within the operational parameter space.

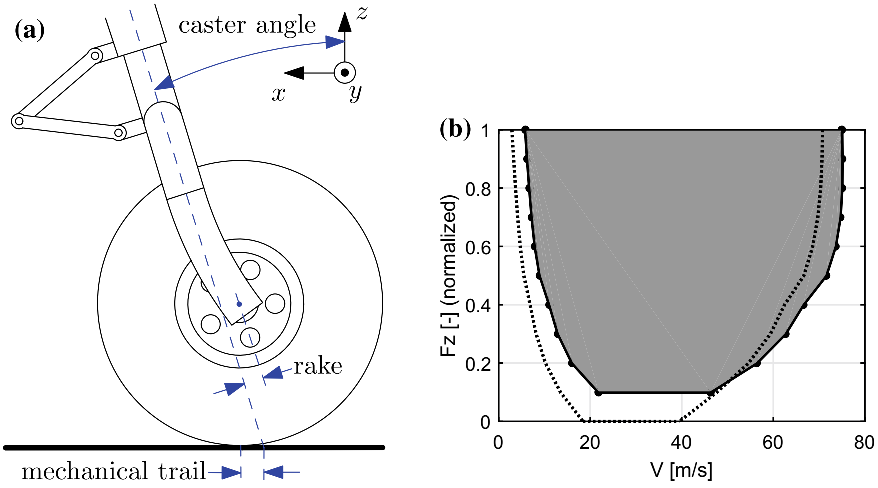

Fig. 7.17 **a** Schematic side view of the bottom part of the nose landing gear, showing the definitions for caster angle, rake, and mechanical trail. **b** Stability boundary for two different rake values. The solid line is 0 mm rake, while dotted line is 15 mm rake. $d_{damper} = 0.03$ in both situations

7.5.2.2 Mechanical Trail Sensitivity Study

Other design parameters that are at the disposal of the landing gear designer, and that can change the shimmy characteristics of a landing gear, are the rake and the caster angle. As indicated in Fig. 7.17a, the rake is defined to be the offset of the wheel center with respect to the steering axis. Both the rake and the caster angle influence the mechanical trail, which is the distance between the point where the steering axis meets the road and the tire-road contact point, and is known to have a large effect on shimmy behavior.

The study model, as analysed so far and as shown in Fig. 7.5, has a rake of 0 mm. This implies that the piston fork is straight. Together with the caster angle of 17°, this results in a mechanical trail of 67 mm. The bifurcation analysis is repeated with an identical landing gear study model, except for the fact that a rake of 15 mm is implemented, by curving the piston fork forward. This changes both the flexible piston stiffness slightly and results in a reduced mechanical trail of 52 mm.

A bifurcation analysis is performed on the model with a rake of 15 mm and the results are compared to those of the 0 mm rake model, which were already shown in Fig. 7.15b. Both results are combined in Fig. 7.17b. In this figure, the unstable domain of the 0 mm rake model is indicated by the shaded surface and the stability boundary of the 15 mm-rake model is indicated by the dotted line.

The results show that, with respect to the original stability domain, the model with an increased rake has an unstable domain that is roughly the same size. However, the unstable domain shifts to slightly lower velocities.

Fig. 7.18 Unstable domain, in gray, of a landing gear with the steering actuator enabled

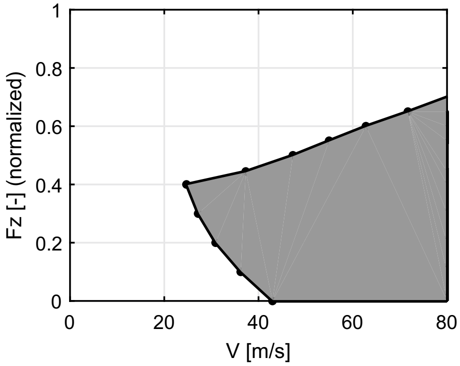

7.5.2.3 Steering Actuator Enabled

In all the analysed situations above, the steering actuator of the landing gear is assumed to be off, as it would be during landing or take-off. In the next situation, the steering actuator is assumed to be on, as it would be during a taxi event at low velocities. In that case, the actuator can be modeled as a linear rotational spring-damper with stiffness 10^4 Nm/rad and damping 5×10^3 Nm s/rad. Opposed to the passive shimmy damping results discussed above, the functionality of the steering actuator has not been reduced, i.e., the actuator is assumed to be fully operational. For this situation, the results of a quasi-2-parameter bifurcation analysis are displayed in Fig. 7.18.

The results show that, even with a fully operational steering actuator, the landing gear shows shimmy. The shape of the unstable domain is drastically different from the parabola-like shape encountered in the previous bifurcation analysis results. In this case, the landing gear only experiences shimmy at higher velocities and lower vertical loads. At a normalized vertical force of 0.4, shimmy already starts to occur at a velocity of 25 m/s. However, this will probably not result in any practical problems, because aircraft velocities during taxiing are on average 10 m/s. Time simulations show that, also in this case, where the dynamics are significantly altered with respect to a situation with a disengaged steering actuator, the critical oscillation starts as a yaw oscillation of the landing gear.

7.6 Conclusions

In this chapter, first a complex, high-fidelity, flexible multibody model of a typical industrial nose landing gear is presented. The model contains many of the modeling elements normally encountered in multibody models used in industry, such as complex tire dynamics, complex geometry, non-linear spring/damper elements, and flexible bodies. Reduced Craig-Bampton mode sets are used to approximate flexible body dynamics. The model is shown to be comparable to a multibody landing gear model used in industry, but with significantly less degrees of freedom, thereby opening possibilities for a bifurcation-based shimmy analysis.

A recently developed simulation framework, that combines AUTO and the Virtual.Lab Motion solver through use of a custom interface with MATLAB, is adapted to perform bifurcation analyses on the landing gear study model. The framework enables the continuation of a branch of (quasi)-static solutions of the multibody model, as function of the horizontal velocity V. By repeating the analysis and varying a second parameter, the vertical normal force F_z, quasi-2-parameter bifurcation diagrams are created.

The practically relevant and safety-critical case of a leaking shimmy damper is considered. The unstable domain, as revealed by a quasi-2-parameter bifurcation analysis, is verified using 30 conventional time simulations. Time-domain steady-state response results are shown to be in accordance with the obtained bifurcation diagram. It is thus shown that it is possible to use the bifurcation analysis framework to analyse the shimmy behavior of complex, high-fidelity multibody models.

A comparison of the computation time reveals that the bifurcation analysis gives a far more detailed view of the stability properties of the model at comparable computational costs, as 20 exact points of the stability boundary are determined. Trying to capture the stability boundary with a comparable accuracy using time-domain simulations would be much more computationally expensive and would be prohibitive in sensitivity studies needed in the context of landing gear design.

Such sensitivity studies are performed to investigate the influence of several design parameters on the bifurcation boundary in the (V, F_z)-parameter space. It is shown that only after severe reduction of the shimmy damper functionality, to less than 5% of its original value, the landing gear will show shimmy within the operational parameter space. Shimmy is more present at higher vertical loads and expands quickly in the (V, F_z)-parameter space if the shimmy damper coefficient is reduced further, indicating the importance of proper shimmy damper operation. Secondly, it is shown that for a model with a decreased mechanical trail, the unstable domain shifts to slightly lower velocities, while its shape and size in the parameter space remain roughly the same. Lastly, in a situation where the steering actuator of the landing gear is turned on, as it would be during taxiing, the additional stiffness in yaw direction leads to drastically different shimmy behavior, mainly present at higher velocities and lower vertical loads.

Acknowledgements The work in this chapter was supported by Siemens PLM Software and Fokker Landing Gear. Their cooperation is gratefully acknowledged.

References

1. Bampton, M.C.C., Craig Jr., R.R.: Coupling of substructures for dynamic analyses. AIAA J. **6**(7), 1313–1319 (1968). https://doi.org/10.2514/3.4741
2. Beckers, C.J.J., Ongüt, A.E., Verbeek, B., Fey, R.H.B., Lemmens, Y., van de Wouw, N.: Bifurcation analysis of landing gear shimmy using flexible multibody models. In: Ambrósio, J. (ed.) 5th Joint International Conference on Multibody Systems and Dynamics (IMSD), 46. Portugal, June, 24–28 Lisboa (2018). http://imsd2018.tecnico.ulisboa.pt/Web_Abstracts_IMSD2018/pdf/WEB_PAPERS/IMSD2018_Full_Paper_46.pdf
3. Coetzee, E., Thota, P., Rankin, J.: Dynamical Systems Toolbox. https://nl.mathworks.com/matlabcentral/fileexchange/32210-dynamical-systems-toolbox (2011). Accessed 14 June 2018
4. Doedel, E., Keller, H.B., Kernevez, J.P.: Numerical analysis and control of bifurcation problems (I): bifurcation in finite dimensions. Int. J. Bifurc. Chaos **01**(03), 493–520 (1991). https://doi.org/10.1142/S0218127491000397
5. Doedel, E.J., Oldeman, B.E.: AUTO-07P: Continuation and bifurcation software for ordinary differential equations. Technical Report, Concordia University, Montreal. http://indy.cs.concordia.ca/auto (2012). Accessed 14 June 2018
6. Haug, E.J.: Computer Aided Kinematics and Dynamics of Mechanical Systems, 1st edn. Allyn and Bacon, 160 Gould Street, Needham Heights, Massachusetts 02194 (1989)
7. Howcroft, C., Lowenberg, M.H., Neild, S., Krauskopf, B., Coetzee, E.: Shimmy of an aircraft main landing gear with geometric coupling and mechanical freeplay. J. Comput. Nonlinear Dyn. **10**(5), 051,011 (2015)
8. Shabana, A.A.: Dynamics of Multibody Systems, 4th edn. Cambridge University Press, Cambridge (2013)
9. Siemens Product Lifecycle Management Software Inc.: Case study—GKN Aerospace Fokker Landing Gear. https://www.plm.automation.siemens.com/pub/case-studies/64181?resourceId=64181 (2017). Accessed 6 Apr 2018
10. Siemens Product Lifecycle Management Software Inc.: LMS Virtual.Lab Motion Online Help (documentation) (2017)
11. Tartaruga, I., Lowenberg, M.H., Cooper, J.E., Sartor, P., Lemmens, Y.: Bifurcation analysis of a nose landing gear system. In: 15th Dynamics Spectral Conference, American Institute of Aeronautics and Astronautics, San Diego, California, USA, AIAA SciTech Forum (2016). https://doi.org/10.2514/6.2016-1572
12. Thomsen, J.J.: Vibrations and Stability, 2nd edn. Springer, Berlin, Heidelberg, https://doi.org/10.1007/978-3-662-10793-5 (2003)
13. Thota, P., Krauskopf, B., Lowenberg, M.H.: Interaction of torsion and lateral bending in aircraft nose landing gear shimmy. Nonlinear Dyn. **57**(3), 455–467 (2009). https://doi.org/10.1007/s11071-008-9455-y
14. Yoo, W.S., Haug, E.J.: Dynamics of articulated structures. Part I. Theory. J. Struct. Mech. **14**(1), 105–126 (1986). https://doi.org/10.1080/03601218608907512
15. Yoo, W.S., Haug, E.J.: Dynamics of flexible mechanical systems using vibration and static correction modes. J. Mech. Trans. Autom. **108**(3), 315–322 (1986b). https://doi.org/10.1115/1.3258733